

Automated glenoid bone loss measurement and segmentation in CT scans for pre-operative planning in shoulder instability

Zhonghao Liu¹, Hanxue Gu², Qihang Li³, Michael Fox⁶, Jay M. Levin⁶, Maciej A. Mazurowski^{2,3,4,5}, and Brian C. Lau⁶

¹Department of Biomedical Engineering, Duke University

²Department of Electrical and Computer Engineering, Duke University

³Department of Biostatistics and Bioinformatics, Duke University

⁴Department of Computer Science, Duke University

⁵Department of Radiology, Duke University

⁶Department of Orthopaedic Surgery, Duke University Medical Center

November 19, 2025

Abstract

Background: Reliable measurement of glenoid bone loss is essential for operative planning in shoulder instability, but current manual and semi-automated methods are time-consuming and often subject to inter-reader variability.

Purpose/Hypothesis: To develop and validate a fully automated, deep-learning pipeline for measuring glenoid bone loss on 3D computed tomography (CT) scans using linear-based, en-face view, and best-circle method. We hypothesized that automated measurements would perform comparable to expert surgeons.

Study Design: Cohort study (diagnosis); Level of evidence, 2.

Methods: Shoulder CT images of 91 patients (average age, 40 years; range, 14–89 years; 65 men) were retrospectively collected between January 2013 and March 2023, along with manually labeled glenoid and humerus segmentations, glenoid rim points, and percentage bone-loss measurements. Our fully automated multi-stage algorithm consists of three main stages: (1) Segmentation, where we developed a U-Net to automatically segment the glenoid and humerus; (2)

anatomical landmark detection, where a second network predicts glenoid rim points; and (3) geometric fitting, where we applied a principal component analysis (PCA), projection, and circle fitting to compute the percentage of bone loss.

Results: The automated measurements showed strong agreement with consensus readings, exceeding surgeon-to-surgeon consistency (intraclass correlation coefficient [ICC] 0.84 vs 0.78). ICC values were 0.71 vs 0.63 for the low-bone-loss subgroup and 0.83 vs 0.21 for the high-bone-loss group ($P < .001$). For the classification task of assigning each patient to low-, medium-, or high-bone-loss severity subgroups, the pipeline's recall (sensitivity) was 0.714 (5/7) for the low-severity group and 0.857 (6/7) for the high-severity group, with no instances of misclassifying low as high or vice versa.

Conclusion: We developed a novel, time-efficient, fully automated, deep learning-based pipeline for glenoid bone-loss measurement on 3D volume-rendered CT. The pipeline shows strong agreement with surgeon measurements, good reliability, and high recall for the low- and high-bone-loss subgroups. Therefore, it may serve as a clin-

ically reliable tool to assist clinicians with preoperative planning for shoulder instability, particularly for screening patients with high bone loss, while still requiring human review for cases of moderate bone loss. We are releasing our model and dataset at <https://github.com/Edenliu1/Auto-Glenoid-Measurement-DL-Pipeline>.

Keywords: glenoid bone loss; deep learning; automated measurement; CT; segmentation; landmark

1 Background

The glenoid fossa is the shallow bony socket on the lateral scapula that articulates with the humeral head, allowing a wide range of arm motion. This mobility comes at the cost of stability[1][2]; the shoulder is therefore especially vulnerable to traumatic dislocation[3]. Approximately 1.7% of the general population has a traumatic shoulder instability, and the recurrence rate is substantial[1][2][4]. In a clinical setting, accurate glenoid bone loss measurement is important for shoulder surgical planning, as an inaccurate measurement may lead to a completely different surgical management for the patient[5]. To illustrate, smaller lesions with low bone loss may require conservative interventions, whereas larger defects may require surgical interventions such as laterjet transfers or allograft augmentations[6].

There are many methods for measuring glenoid bone loss, 2D, 3D, linear-based, area-based, and volume-based, using CT or MRI[6][7][8][9]. Here, our study focuses on 3D-reconstructed CT linear-based en-face views with a best-fit circle method, as it's the most popular method surgeons use for surgical planning[10][11]. The detailed procedure is as follows: (1) On an en-face view of a 3D bone rendered CT image, fit a circle to the glenoid 3 to 9 o'clock inferior contour. (2) Draw a line from the glenoid defect to the anterior margin of the circle (B). (3) Compute bone loss using: $(B/A(\text{diameter})) \times 100\%$. The most popular approaches for measuring glenoid bone loss include software-assisted (semi-automated) methods and fully manual measurements. Semi-automated tools typically standardize image preprocessing and segmentation but still rely on the clinician to select

the en face view and fit the circle, and fully manual measurement is based on the doctor's best judgment. The weaknesses of both methods include extensive human labor and time, along with poor interrater variability (low agreement between doctors in en face view choice and bone-loss measurement)[12][13][14].

Many ideas have been proposed to solve these weaknesses; only a few are fully automated. Haimi's method segmented the glenoid using a Hounsfield units (HU) threshold within an interval, applied PCA to reorient the glenoid slices to an en-face view, and fit a circle using a few predetermined clock positions on the glenoid segmentation [15]. The flaws of this method are that HU-based segmentation may inaccurately include pixels of arthritis that fall within the interval; PCA is not the optimal solution for finding the en-face view because it can be largely influenced by cupping bone loss, which is discussed later in the paper; and the bone loss measurement was computed over a selected 2D slice of a CT scan, which many studies have found can underestimate the bone loss[9]. Zhao et al.'s method requires a healthy contralateral side for the bone loss computation, while many CT scans include only one side[16].

We propose a fully automated, deep learning-based pipeline for 3D CT glenoid segmentation and measurement of glenoid bone loss using a linear-based, en-face view and the best-fit circle method. The glenoid bone is obtained using a deep learning model that is not subject to shoulder arthritis. A better approach is used to find the en face view, relying only on information from the intact side of the glenoid rim. Bone loss is measured on a 3D bone-rendered image rather than a 2D slice to avoid underestimation. A healthy contralateral side is not needed for this pipeline. Moreover, we assessed agreement using intraclass correlation coefficients (ICCs) to ensure that measurements to quantify inter-rater agreement across raters (algorithm vs. gold standard), which matters for understanding reliability of algorithm for making surgical decisions. We also analyzed three bone-loss severity subgroups to approximate surgical decision management. We found that our pipeline for automating glenoid bone loss achieves higher agreement and correlation than the human baseline and demonstrates good reliability, especially in subgroups

with low and high severity of bone loss. It is clinically reliable for assisting physicians in preoperative planning.

The purpose of this study is to develop and validate a fully automated, deep-learning pipeline for measuring glenoid bone loss on 3D scans using glenoid rim points, geometric fitting, and a principle component analysis, projection, and circle fitting to compute the percentage of bone loss. We hypothesize that automated measurements would demonstrate comparable performance to surgeon measurements.

2 METHODS

2.1 Patient Data

This study was conducted in accordance with ethics guidelines and received approval from the institutional review board (Pro10080765). Informed consent was waived due to the retrospective design of the study.

Our dataset of 3D shoulder CTs were retrospectively collected from patients between January 2013 and March 2023. The training dataset was sampled from this entire dataset shoulder CT dataset and was screened and labeled by an orthopedic surgeon (over 15 years of experience). The test dataset was sampled from a cohort within the same dataset but comprising healthy patients and patients who had undergone shoulder stabilization surgery, and it was screened and labeled by two experienced surgeons. Exclusion criteria included: (1) patients with posterior glenoid bone loss, (2) patients with a shoulder implant, and (3) patients with severe arthritis (measurement not feasible for physicians).

Different degrees of glenoid bone loss require different preoperative planning. There is a general consensus that glenoid defects beyond roughly 20% of the glenoid diameter should be managed with a bony augmentation procedure – most commonly the Latarjet coracoid transfer or a similar bone graft technique – rather than with labral repair alone[17][18]. Therefore, we considered it important to test the algorithm in groups representing different levels of bone loss: < 13%, 13 – 20%, and > 20%.

We stratified the screened dataset and randomly

divide it into a 20% training data set and a 80% test data set, resulting in 21 patient CTs in the test data set and 77 in the train data set, as shown in Table 1. Demographic characteristics and scanne’s information of the training and testing cohorts can be found in Table 2.

2.2 Automated Glenoid Bone Loss Measurement Pipeline

We introduce a fully automated, end-to-end deep learning-based pipeline for segmenting the glenoid articular surface and measuring bone loss on 3D reconstructed CT using linear-based, en-face view, and best-fit circle method. The pipeline follows the same procedure applied by the clinician, as described in the introduction. Below is a brief pipeline description: 1. The trained deep learning segmentation model reads the shoulder CT scan and outputs the left/right glenoid and humerus bone loss labels. 2. The glenoid bone label is flipped along the depth dimension if detected as a Right glenoid. 3. The trained Rim-UNet reads the preprocessed binary segmentation map from the segmentation model and predicts the rim point sets. The predicted rim points are then back-registered to the original segmentation map 4. Given 3-D rim-skeleton points, we estimate a best-fit plane via SVD/PCA on the point cloud, taking the direction normal to the top two largest variance directions as the en-face view. 5. Glenoid segmentation and rim points are projected onto this plane. A 2-D geometric circle is fit by minimizing the radial least-squares objective $J(c, r) = \sum_i(\|p_i - c\|_2 - r)^2$ using BFGS (c = center of circle coordinate; r = radius of the circle; p = rim point sets). Based on the clinical suggestion of the diameter of the fitted circle usually being 2/3 of the glenoid height, we did an optimization test using a grid search around the hyperparameter of 2/3 on the train set. Here we explicitly set the radius to be 0.6955/2 based on the analysis (Fig. 3). 6. Bone loss is measured by dividing the glenoid defect (B) by the diameter of the fitted circle (A): $(B/A) \times 100\%$. Following Hami’s method, determining B, many radial lines are drawn from the glenoid defect to the anterior margin of the circle, and the longest line represents the length of

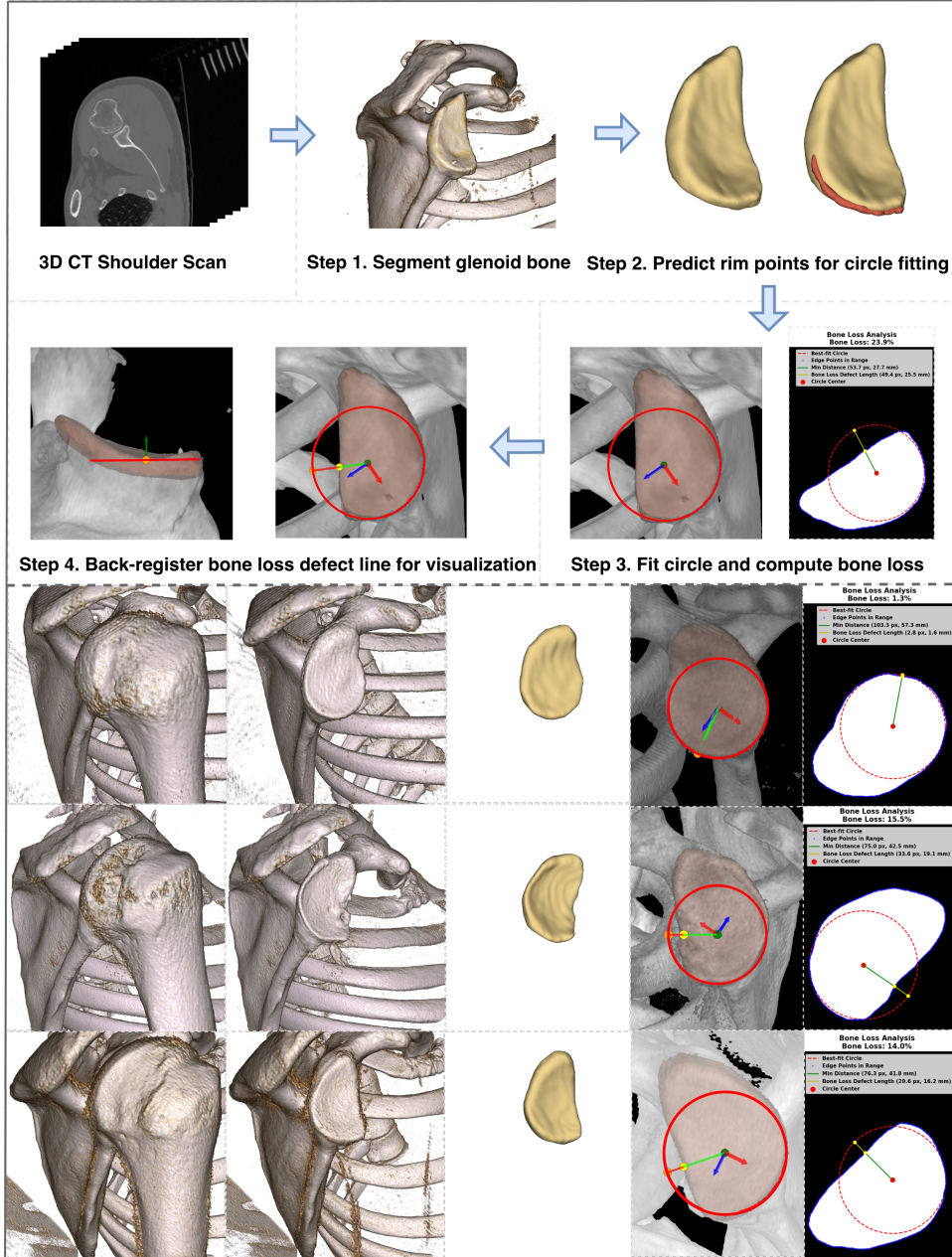


Figure 1: Pipeline for automated glenoid bone loss measurement. (1) The segmentation model delineates the glenoid articular surface; (2) RIM-UNet reads the segmentation mask and predicts rim points; (3) singular value decomposition (SVD) estimates the rim-plane normal, defining the en face view; (4) the segmentation mask and rim points are projected onto the en-face plane; and (5) a 2D circle is fitted to the rim points. Bone loss is computed as $100 \times B/A$, where B is the glenoid-defect length and A is the fitted-circle diameter.

Three more examples for demonstration.

Table 1: Distribution of anterior glenoid bone-loss categories

Bone-loss category	Train (n = 60)	Test (n = 21)	Total (n = 81)
< 13.5 %	26 (43%)	7 (33%)	33 (41%)
13.5–20 %	15 (25%)	7 (33%)	22 (27%)
> 20 %	19 (32%)	7 (33%)	26 (32%)
Total	60 (100%)	21 (100%)	81 (100%)

the glenoid defect [15]. A general workflow of this fully automated pipeline is outlined in the flowchart provided in Figure 1.

2.3 Data Annotation

Segmentation Annotation: The annotation of the scapulae and humerus bones for the entire dataset was completed under the guidance of an orthopedic surgeon with more than 10 years of experience in sports medicine. We segmented the thin layer at the top of the glenoid fossa, which experts would consider a part to measure bone loss in the glenoid after finding the en-face view. All segmentation annotations are refined and approved by one surgeon for the training dataset and two for the test dataset.

Landmark annotation: A varied number of landmarks are selected on the surface of the posterior inferior rim on the annotated binary segmentation mask of the glenoid bone in 3D slicer, which will be used for training the model for circle fitting. The rim curve doctor refers to for circle fitting is shorter for patients with a lot of glenoid bone loss, but longer for patients with little bone loss. Therefore, we need to train a model that can output data accommodating different amounts of bone loss, which can output different sets of rim points. The instruction for selecting landmarks that best represent the intact posterior/inferior glenoid rim is given to researchers and surgeons.

1. Rotate the glenoid surface mask until the en-face view is normal to the labeler [10]
2. Select a landmark from what is considered 3 o’clock based on the labeler’s experience that coincided with the intact posterior-inferior rim [10]

3. Following the outermost rim, select the landmark until the curve meets the inferior defect aspect [19]

Similar to segmentation annotation, we manually label the landmark, which is then refined and approved by an experienced surgeon. One surgeon refined and approved the train dataset, while two surgeons refined and approved the test dataset.

2.4 Ground-Truth Generation

The ground truth for the segmentation model does not require any pre-processing, as the foreground binary mask can be used directly for training. In contrast, the ground truth for the rim model requires pre-processing, as there isn’t a fixed number and location of landmarks that can represent the curve for circle fitting across different level of bone loss. To enable the model to learn from the selected landmarks and generate information that can be easily post-processed for circle fitting, we follow these steps: 1. For consistency, the landmarks for each case were resampled to 30 landmarks on the 3D slicer. 2. Using the Markups to Model module in 3D slicer, the landmark markup is converted to a tube with a radius of 1.00 mm with a curve-type cardinal spline 3. The rim tube is then skeletonized into a thin curve with a thickness of 1 pixel. An isotropic 3D Gaussian kernel $\sigma = 1$ mm is applied to the thin skeletonized curve to regress a heatmap in the range of [0,1].

Additional pre-processing is used to inject an inductive bias and reduce data efficiency, leveraging the intrinsic geometry of the glenoid fossa. We believe that this can accelerate learning with limited data. To begin with, we applied PCA in each plate-shaped

Table 2: Distribution of demographics and scanner characteristics

Characteristic	Train (n = 61)	Test (n = 21)	Total (n = 92)
Sex			
Male	42 (69%)	16 (76%)	65 (71%)
Female	19 (31%)	5 (24%)	27 (29%)
Age (years)			
Mean \pm SD	44.3 \pm 22.4	28.5 \pm 13.1	39.6 \pm 20.4
Range	[14, 89]	[15, 65]	[14, 89]
Missing	2	1	3
Weight (kg)			
Mean \pm SD	81.8 \pm 16.9	83.7 \pm 16.4	83.0 \pm 16.7
Range	[45.7, 133.0]	[59.0, 113.4]	[45.7, 133.0]
Missing	24	3	33
Scanner model			
SOMATOM Force	18 (30%)	9 (43%)	31 (34%)
Discovery CT750 HD	15 (25%)	10 (48%)	26 (28%)
SOMATOM Definition Flash	10 (16%)	2 (10%)	16 (17%)
Revolution HD	10 (16%)	0 (0%)	11 (12%)
SOMATOM Definition AS	4 (7%)	0 (0%)	4 (4%)
LightSpeed VCT	3 (5%)	0 (0%)	3 (3%)
Optima CT660	1 (2%)	0 (0%)	1 (1%)
Total patients	61 (100%)	21 (100%)	92 (100%)

glenoid mask and rotated the volume so that the glenoid articular surface faces the z-axis, reducing the depth of the mask. With this, we can reduce the dimension of the glenoid binary mask from 112^3 voxels to $48 \times 112 \times 112$. Second, all right shoulders are flipped across the sagittal plane so that they appear as a left shoulders, making it mirror invariance. These steps standardize laterality and reduce dimensionality, allowing the network to learn from a smaller, more simpler feature space.

2.5 Model’s Architecture

Segmentation backbone (nnU-Net / TotalSegmentator). We only have 61 volumes in training data, which is considered a low number of images for deep learning training. To address this data scarcity, we conducted a two-stage fine-tuning of the public TotalSegmentator model, built on nnU-Net [20] [21].

Transfer learning is a highly data-efficient approach for training models in small subsets of data [22], and TotalSegmentator is a multi-label segmentation model trained on 104 anatomic structures across 1204 CT examinations, encompassing the scapula and humerus bones. We believe that fine-tuning TotalSegmentator can transfer its rich anatomical knowledge of these bones in the CT domain to our task of segmenting four target labels: left/right glenoids and left/right humerus bones.

The first stage of fine-tuning involves fully utilizing TotalSegmentator’s large CT dataset and learning the coarse bony context of the scapula and humerus, which can later be refined on the substructures of the glenoid bone. We filtered out CTs that do not include the scapula label for the training dataset, leaving 849 training data. We trained the 3D full-resolution nnU-Net

from TotalSegmentator (CT) using the trainer `nnUNetTrainerNoMirroring`, following no mirroring specification in its original training plan. Initialization used the public TotalSegmentator checkpoint `Dataset294_TotalSegmentator_part4_muscles`, fold 0 (final checkpoint). Auto-planning selected 1.5 mm isotropic spacing, a 128^3 -voxel patch size, and a batch size of 2. We set the base learning rate at 10^{-4} for fine-tuning; all other hyperparameters, augmentations, and schedules followed nnU-Net defaults.

In the second stage, we further fine-tuned the model on our subdata set to capture finer substructures, as described on the glenoid articular surface[23]. We collected a smaller dataset under the guidance of an orthopedic surgeon, comprising 98 CT scans and their corresponding left/ right glenoid articular surfaces and humerus bone loss, as shown in Table 1. The training plan used to fine-tune the first-stage model is identical to the one used in the first stage. We used the same loss function for both stages, $L = LCE + LDICE$, which combines entropy loss and the dice loss. We will release the exact plan/config JSON, trained weights, and scripts for full reproducibility (GitHub link coming up).

Rim-UNet: Heatmap regression model for circle fitting. Manual measurement of glenoid bone loss in 3D CT scans by doctors in general requires (1) finding an en-face view, (2) projecting the 3D image in that direction, and (3) drawing a best-fit circle to the outermost rim/contour [10]. This pipeline would require solving two values: the direction vector at which a doctor would think makes the glenoid surface normal to their eye(en-face view), and the rim curve at the intact glenoid contour (excluding bone loss areas), which they refer to for circle fitting. Inspired by the Constellation Technique (CST), which labels the glenoid rim regardless of en face orientation, we introduce a novel approach to train a deep learning model for the best-fit circle on the glenoid contour, solving both tasks above with a single model and a small dataset. Rim data for training is selected first, reorienting the en-face view, and then, on that plane, select the outermost rim, encompassing information about both rim and the en-face view coordinates. Therefore, RimNet can skip the en-face view localizing

and directly predict the outermost rim contour that the doctors use for circle fitting in 3D space. The en-face view direction vector can then be calculated with SVD on the curve points.

The RimNet is adapted from the structure of a vanilla U-net tailored for the heat-map regression thin-curve task. In addition to a basic encoder-decoder structure, we used strided convolution (2, 2, 1) to replace the max-pooling for downsampling in the first two stages to preserve the details of the plane for our anisotropic medical images [20]. Moreover, for each convolution, we use Instance Normalization for medical images in small batches [24] and LeakyReLU activations with $\alpha = 0.01$ to preserve all gradients flowing to the prediction of our sparse target output [25]. We used adaptive wing loss for our landmark localization task, as a greater penalty is needed for medium to small errors. [26][27].

$$AWing(y, \hat{y}) =$$

$$\begin{cases} \omega \ln \left(1 + \left| \frac{y - \hat{y}}{\epsilon} \right|^{\alpha-y} \right), & \text{if } |y - \hat{y}| < \theta, \\ A |y - \hat{y}| - C, & \text{otherwise.} \end{cases} \quad (1)$$

where $A = \omega(1/(1 + (\theta/\epsilon)^{\alpha-y}))(\alpha - y)((\theta/\epsilon)^{\alpha-y-1})(1/\epsilon)$ and $C = (\theta A - \omega \ln(1 + (\theta/\epsilon)^{\alpha-y}))$. We heuristically use parameters based on the Adaptive Wing Loss paper: $\omega = 16$, $\epsilon = 1$, $\theta = 0.5$, $\alpha = 2.1$ [27]. We used Adam to optimize training and ReduceLROnPlateau built in PyTorch to dynamically adjust the learning rate [28]. We use the symmetric Chamfer distance between the predicted and reference set of skeleton points as a metric to evaluate the performance of the model $CD(A, B) = \frac{1}{|A|} \sum_{a \in A} \min_{b \in B} \|a - b\|_2 + \frac{1}{|B|} \sum_{b \in B} \min_{a \in A} \|b - a\|_2$ [29][30]. The predicted heat maps are binarized at 0.3 (threshold chosen in the validation set), forming a tubular rim volume that is then skeletonized to a 1-voxel-wide curve using the 3-D thinning method of Lee et al.[31]. Chamfer distance is computed in millimeters via the voxel spacing.

2.6 Experimental Plan

To evaluate the performance of the proposed deep learning pipeline for glenoid bone measurement, we designed a set of experiments focusing on (i) segmentation accuracy, (ii) accuracy of the en-face view plane computation, (iii) accuracy of curve on the intact posterior inferior contour of the glenoid on en-face view, and (iv) accuracy of the measurement of glenoid bone loss. We tested the result predicted by the pipeline on our test data set across three different levels of bone loss: < 13.5%, 13.5% < loss < 20%, and > 20%.

Experiment 1: Glenoid Articular Surface and Humerus Bone Segmentation

Segmentation of the articular surface of the glenoid and humerus bone is compared between the prediction of the segmentation model and manual measurements of two clinicians in three different levels of bone loss. The dice coefficient is used as the accuracy metric.

Experiment 2: Curve on the Intact Contour of the Glenoid

This experiment compares the chamfer scores of the point sets of glenoid rim generated by the algorithm and the mean point sets of two clinicians.

Experiment 3: En-face View

This experiment compares the angular difference between the algorithm-predicted en-face view and consensus direction to the half angular difference between two doctors. To make a fair comparison, we first compute angular difference between two doctors $\phi = \arccos(\hat{d}_1 \cdot \hat{d}_2)$, then the human error would be $\approx \phi/2$ because a single doctor's error is $\phi/2$ from $\hat{\mu}$. Algorithm error involves the angular difference between the direction vector predicted by the algorithm and a consensus unit direction from the two doctors, same direction vector by $\phi = \arccos(\hat{d}_1 \cdot \hat{d}_2)$, but in a different form, $\hat{\mu} = \frac{\hat{d}_1 + \hat{d}_2}{\|\hat{d}_1 + \hat{d}_2\|}$. Then the algorithm's angular error would be $\theta_A = \arccos(\text{clip}(\hat{a} \cdot \hat{\mu}, -1, 1))$.

Experiment 4: Glenoid Bone Loss

This experiment evaluated algorithm-predicted glenoid bone loss against physician measurements, using human-to-human measurements as the baseline, throughout the whole patient cohort, and within three subgroups of severity of bone loss. We used mean absolute error (MAE) to quantify error magnitude, the Pearson correlation coefficient for correlation analysis,

a two-way mixed-effects, absolute-agreement, single-measurement intraclass correlation coefficient (ICC) for agreement, Bland–Altman analysis to assess systematic bias, and a confusion matrix to evaluate the model's classification performance.

3 RESULTS

We conducted four experiments that evaluated the automated glenoid bone loss pipeline in our test data set.

3.1 Experiment 1: Evaluation of Glenoid Articular Surface Segmentation

The segmentation predicted by the model was compared with the manual labels from two clinicians. The average Dice similarity coefficient was 0.875 ± 0.044 for the glenoid (Q1–Q3: 0.847–0.896; range: 0.762–0.930; $n = 21$). For the humerus, it was 0.987 ± 0.006 (Q1–Q3: 0.981–0.992; range: 0.972–0.994; $n = 21$).

3.2 Experiment 2: Evaluation of Predicted Rim on the Intact Posterior Contour of the Glenoid

We evaluated the accuracy of the rim points predicted by Rim-UNet using the bidirectional Chamfer distance between the predicted and ground-truth glenoid rim skeletons (in mm). The Chamfer distance estimates how similar the predicted rim point set is to the set annotated by the clinician on the glenoid surface. The mean nearest-neighbor distance was 1.37 ± 0.58 mm, with most cases having distances < 1.17 mm.

3.3 Experiment 3: Assessment of En-face Direction Vector

We evaluated the en-face view of the glenoid computed by the algorithm against manual selections from two clinicians. The mean of a doctor's angular error to the consensus on en face view is $4.94^\circ \pm 1.86^\circ$ (95% CI: 4.09° – 5.78°), while the algorithm's angular error to consensus is $7.85^\circ \pm 3.99^\circ$ (95% CI: 6.03° – 9.67°).

Table 3: Interobserver reliability between the automated pipeline and manual measurements of glenoid bone loss^a

Comparison	Category	ICC (95% CI)	Pearson r	n
Doctor 1 vs Doctor 2	Human Baseline	0.7822 (0.5292, 0.9075)	0.7940	21
Algorithm vs Doctor 1	Algorithm vs Doctor	0.7842 (0.5329, 0.9084)	0.7949	21
Algorithm vs Doctor 2	Algorithm vs Doctor	0.8036 (0.5695, 0.9171)	0.8088	21
Algorithm vs Consensus	Algorithm vs Consensus	0.8382 (0.6370, 0.9325)	0.8460	21

^aValues are ICC(A,1) with 95% confidence intervals. Pearson r is the Pearson correlation coefficient. Consensus is the mean of doctors' measurements. n indicates the number of paired measurements.

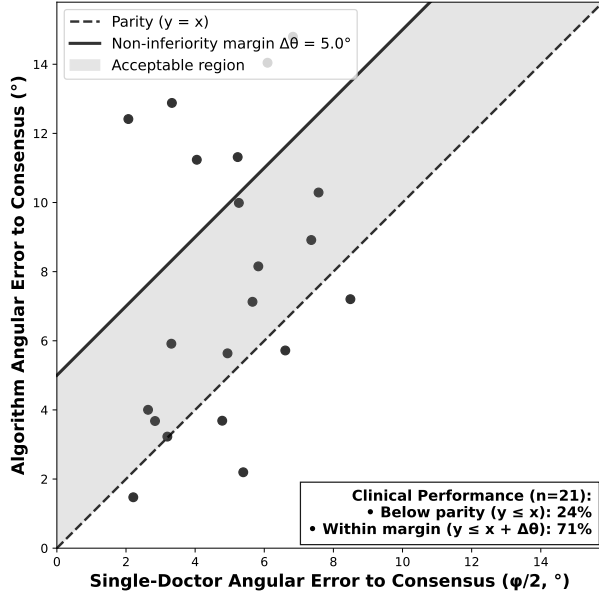


Figure 2: Scatter plot comparing the algorithm-predicted en-face direction to the doctor baseline. Each point is one case. The X-axis is the error of one doctor's measurement to the consensus(two doctors' mean); the Y-axis is the predicted angular error to the same consensus. The dashed diagonal ($y=x$) marks parity with a typical single doctor; points below this line have lower error than a single doctor. The dotted line ($y=x+5^\circ$) indicates the pre-specified non-inferiority margin; points in the gray region at or below this line are *within the allowable tolerance*.

While the mean error of algorithm-consensus pair is higher, of 21 observation analyzed, 24% demonstrated algorithm performance below parity ($y \leq x$), and 71% fell within the clinically acceptable non-inferiority margin of 5° ($y \leq x + \Delta\theta$).

3.4 Experiment 4: Glenoid Bone Loss

We evaluated the accuracy and reliability of the fully automatic end-to-end pipeline. The algorithm demonstrated a mean absolute error of $4.28 \pm 3.38\%$ (median = 3.79%) when compared with the consensus ground truth (the mean of two expert assessments). Using Pearson's correlation coefficient, we assessed the correlation between the pipeline's predicted bone loss and the clinician's measurements on the test set. Correlation between the algorithm and the consensus was $r = 0.846$ with $p < 0.001$, compared with the inter-rater correlation $r = 0.794$, $p < 0.001$, showing a stronger linear correlation

Table 3 presents two-way mixed-effects, absolute-agreement, single-measure intraclass correlation coefficient ICC(A,1)(Table 3). Algorithm agreement with each clinicians was similar or slightly higher than the doctor-to-doctor baseline. Moreover, the algorithm achieved good reliability overall against consensus, slightly higher than the human-human baseline (ICC 0.84 vs 0.78) with an absolute increase of 0.06.

Intraclass correlation coefficient was also estimated on three bone loss severity subgroups (Table 4). Algorithm's agreement was higher than the human-human baseline for all subgroups except for the moderate bone loss subgroup. In low bone loss group algorithm against concensus has ICC higher than human base-

Table 4: ICC(A,1) by bone loss severity subgroup^b

Group	Comparison	Category	ICC (95% CI)	n
Low Bone Loss (<13.5%)				
	Doctor 1 vs Doctor 2	Human Baseline	0.6259 (-0.2405, 0.9372)	7
	Algorithm vs Doctor 1	Algorithm vs Doctor	0.6821 (-0.1460, 0.9481)	7
	Algorithm vs Doctor 2	Algorithm vs Doctor	0.6638 (-0.1786, 0.9446)	7
	Algorithm vs Consensus	Algorithm vs Consensus	0.7091 (-0.0944, 0.9532)	7
Moderate Bone Loss (13.5–20%)				
	Doctor 1 vs Doctor 2	Human Baseline	-0.1439 (-0.8093, 0.6832)	7
	Algorithm vs Doctor 1	Algorithm vs Doctor	-0.0664 (-0.7804, 0.7228)	7
	Algorithm vs Doctor 2	Algorithm vs Doctor	-0.1190 (-0.8003, 0.6965)	7
	Algorithm vs Consensus	Algorithm vs Consensus	-0.0917 (-0.7902, 0.7104)	7
High Bone Loss (>20%)				
	Doctor 1 vs Doctor 2	Human Baseline	0.2171 (-0.6407, 0.8338)	7
	Algorithm vs Doctor 1	Algorithm vs Doctor	0.5190 (-0.3842, 0.9146)	7
	Algorithm vs Doctor 2	Algorithm vs Doctor	0.7619 (0.0208, 0.9626)	7
	Algorithm vs Consensus	Algorithm vs Consensus	0.8326 (0.2132, 0.9746)	7

^bValues are ICC(A,1) with 95% confidence intervals. Consensus is the mean of doctors' measurements. n indicates the number of paired measurements in each subgroup.

line (ICC 0.71 vs 0.63). In moderate bone loss group agreement across all comparisons are near 0, which shows either no correlation between raters or that the variance between patients are too small. Importantly, in high bone loss group human baseline showed a poor reliability while algorithm-clinician showed a much higher agreement, especially that algorithm-consensus showed a good reliability (ICC 0.21 vs 0.83), an absolute increase of 0.62 (62 percentage points; 383.5% relative).

Bland–Altman agreement for glenoid bone loss from the algorithm showed minimal systematic bias versus the clinician consensus (bias: -0.997%). Relative to the human-to-human baseline, the algorithm exhibited similar bias and a narrower spread of differences (LoA width 21.33 % vs 25.24 %; absolute difference 3.91 %). The algorithm's SD of differences was correspondingly lower (5.44 vs 6.44 %)(Fig 4).

A confusion matrix was used to evaluate the ability of the pipeline to classify the severity of bone loss against the consensus' of the physicians (Fig. 5). The Per-class recall (sensitivity) was 0.714 (5/7)

for Low, 0.286 (2/7) for Moderate, and 0.857 (6/7) for High. Misclassifications were predominantly between adjacent categories (Low↔Moderate: 6 cases; Moderate↔High: 2 cases), with no Low↔High errors. For the clinically important High (> 20%) class, recall was 0.857; that is, 6 of 7 High cases were correctly identified and the remaining case was labeled Moderate. The Moderate class had the lowest recall among all groups.

4 DISCUSSION

The most important finding in this study is that (1) a computer vision and deep learning-based algorithm pipeline can be used to reliably automate the measurement of glenoid bone loss on 3D CT scans. (2) Our algorithm and pipeline can be a clinically reliable tool in assisting pre-operative planning in shoulder instability, especially in screening high bone loss ($\geq 20\%$) as a classification model. (3). The segmentation model in the pipeline is also clinically reliable in subtracting the humerus bone and preparing the glenoid bone

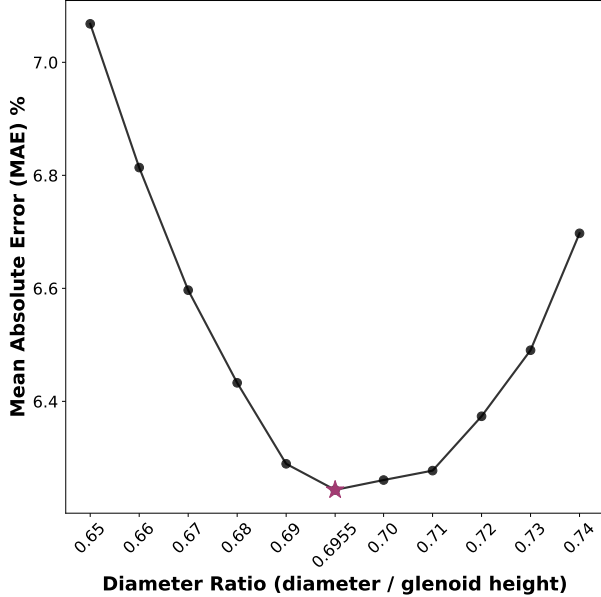


Figure 3: Optimization of Diameter Ratio for Glenoid Bone Loss Prediction on Training Dataset. The X-axis represents the diameter ratio (fitted circle diameter divided by glenoid height) tested across 11 values from 0.65 to 0.75; the Y-axis represents the mean absolute error (MAE, %) in bone loss prediction. The purple star (*) marks the optimal diameter ratio of 0.6955, which achieved MAE = 6.24%. For comparison, the unconstrained fitting method achieved MAE = 8.81%.

segmentation for glenoid bone-related assessment. Additionally, the current automated pipeline can reliably identify true en-face view.

In our analysis of bone loss, our computer vision and deep learning-based pipeline demonstrated higher agreement and correlation with fellowship-trained orthopaedic surgeon measurements compared to the inter-rater baseline between surgeons. It is much better than the human baseline in the high bone loss group (ICC 0.83 vs. 0.22) in reliability. It shows minimal systematic bias and a smaller spread of differences than the human baseline, achieving 71.4 and 85.7 in classifying low and high bone loss groups, respectively, and without any instances of misclassifying low as high or vice versa. The correlation and classification

in the moderate bone loss group are weak, but are consistent with the human baseline. All of which suggests that our computer vision-based deep learning method can reliably automate the measurement of glenoid bone loss in CT scans. Our pipeline is clinically reliable for quantitative measurements and effectively identifies cases of high bone loss, although we recommend human review for cases within the 13.5% to 20% "gray zone." It is important to note that in the gray zone- that clinical surgeon decision making remains gray as well. The current algorithm can trigger surgeons that bone loss is within this zone and requires greater scrutiny as would be the case with manual measurements. In areas of large bone loss- the algorithm accurate measures bone loss which can allow surgeons to reliability plan bony augmentation techniques.

The humerus bone segmentation dice score of 0.9866 ± 0.0059 demonstrated that our segmentation model can be an excellent tool for humerus bone subtraction and, therefore, a great tool to help visualize the glenoid bone. As shown in Figure 1, the humerus bone is completely removed, leaving no residual bone fragment and a complete view of the glenoid bone. It is important to note- that current clinical CT 3D protocols require manual segmentation to remove humerus and create 3D rendered glenoid/scapula images. Based on the reliable bone loss result demonstrated in the pipeline in this study and the fact that the pipeline is clinically reliable in analyzing glenoid bone loss, we believe it also proves that the segmentation model, which is an essential part of the pipeline, is also reliable in helping to make clinical decisions. This segmentation model can be a valid tool for pre-operative planning in shoulder instability.

A lower glenoid bone segmentation score does not necessarily mean that the segmentation model performance is poorer in the glenoid bone. However, it could mean that we do not have a better segmentation metric for evaluating just part of the glenoid bone on the surface toward the joint side that we emphasize. There is a 5% favor in the humerus bone dice score. This difference is expected, as the humerus bone has an enclosed structure that can be easily annotated. In contrast, the glenoid articular surface has a much gray zone defining the opposite side to the articular

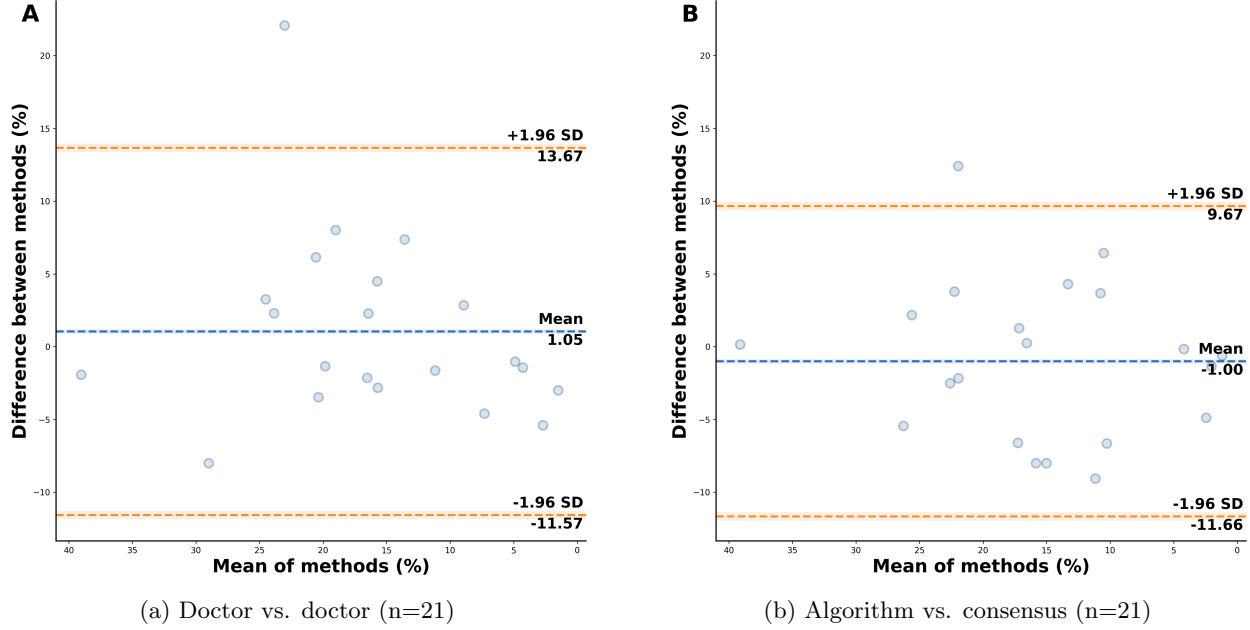


Figure 4: Bland–Altman plots showing agreement between two doctors alongside agreement between the algorithm and consensus measurements.

glenoid surface, where doctors will not have a clear consensus. However, this ambiguity on the other side does not affect the accuracy of the pipeline, as we would only be using the actual side for rim points set finding (see Fig. 1)

The chamfer distance of the rim points between the algorithm’s prediction and the doctor’s consensus indicates strong agreement between the predictions and the clinician’s labels for the rim location on the glenoid surface. Most patients show a distance of less than 1.17 mm, which is minimal compared to the surface area of the glenoid. This shows a good foundation for fitting the circle to these points on the rim for the prediction of bone loss.

Finding an en-face view is challenging, as there is no clear definition of it in clinical settings. We defined the mean of two fellowship trained surgeons directions as consensus and compared the angular error of both the single doctor and the algorithm. Although only 24% of patients show lower error than a single doctor, 71% fell within the clinically acceptable non-inferiority

margin of 5° ($y \leq x + \Delta\theta$), suggesting that while the algorithm generally exceeds inter-observer variability, it remains within a clinically tolerable range for the majority of cases.

4.1 Why not PCA / largest projected area?

Many studies have discussed using PCA or the largest surface area to compute an en-face view to measure glenoid bone loss, either manually or with computer-assisted; however, we found that this approach can be unreliable in cases with severe bone loss (Fig. 6). The cases of high bone loss are the exact scenarios where exact bone loss calculations are needed to appropriate size and plan for bony augmentation. In computer-assisted measurement, this process typically involves segmenting the glenoid bone first, followed by the application of PCA or the largest projected area method. Zhang’s study orients the camera along an initial vector and then rotates to find the plane that

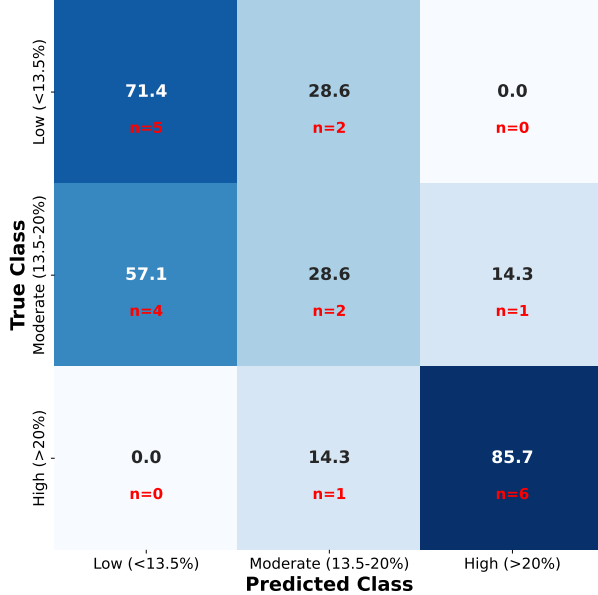


Figure 5: Confusion matrix for the algorithm-predicted glenoid bone loss measurement against the doctor’s consensus. The predicted class axis represents the algorithm’s classification, and the true class represents the doctor’s consensus. Accuracy is centered in each box, and the number of samples is categorized below.

yields the maximum projected area, thereby finding the true en-face view [32]. Haimi’s method requires using PCA to find the plane that gives the maximum variance on the glenoid segmentation, and the en-face view is normal to this plane[15]. This makes sense because the intrinsic surface of the glenoid bone is generally flat. If you have a good segmentation of the glenoid bone articular surface, it should give you the direction vector identical to the en-face view. However, as shown in Figure 6, in a case of severe bone loss the en-face view computed with PCA is not even close to the true en-face view. Due to intrinsic patterns of bone loss, some bone loss occurs not only on one side at the edge but in the center; In this case, it is not only anteriorly but also from top to bottom in the center. This central (cavitory) glenoid erosion is commonly referred to as a glenoid cup[33]. When

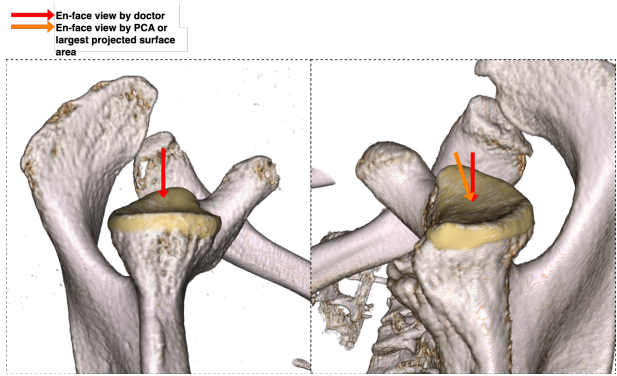


Figure 6: Comparison between en-face view computed on glenoid with minimal bone loss and high bone loss. Left image shows a healthy intact glenoid bone; Right image shows a glenoid bone with high bone loss. True direction vector selected by doctors are shown in red arrow; direction vector computed by PCA and largest projected surface area is shown in orange arrow.

a patient experiences bone loss that occurs both on the side and in the center, the articular surface can erode to one side, leading the PCA and the largest projected surface to lean in that direction as well, causing the view of the face to deviate from the expected position. Based on our observation, this type of bone loss isn’t uncommon, therefore emphasizing that the computation of en-face view cannot rely on PCA or surface area. Our method utilized topological and anatomical information on the posterior side of the glenoid that is invariant to any type of bone loss, the rim edge points on the posterior side, enabling us to find the same en-face view, regardless of different bone loss types.

4.2 Rationale for our approach

Deep learning based methods generally perform the best when trained to specialize in one specific task. Still, we did not optimize the model to output the bone loss, but a segmentation mask and rim points for interpretability in a clinical setting. By training a multi-stage model, one to predict segmentation of glenoid and humerus bone, another to predict rim points where a constrained circle fitting algorithm fits

to for bone loss, it can give surgeons an better grasp at each step as each step imitates exactly what they do in the bone loss measurement guideline: determine what is glenoid and humerus, subtract humerus, determine where is the rim they need to use for circle fitting. With a fully end-to-end deep learning model that maps a CT scan to bone loss regression directly in a black-box framework, not only can we not evaluate each step of the guideline, but there is also less interpretability. We believe our pipeline has a good balance in regressing bone loss and providing interpretability and visualization for the clinical setting.

One thing to address is Rim-Unet’s ability to learn the representation of the en-face view and the glenoid rim for circle fitting within a single model. We made this possible because of our data collection method. We first ask the surgeon to reorient the glenoid articular surface to the en-face view, which is normal to the screen. Then, on this plane, surgeons’ are required to select the rim points containing the plane’s spatial information. Therefore, the models are trained to find rim points already containing the en-face view information. To illustrate this concept, imagine drawing the contour of a bottle in a 3D space from a fixed angle. The paint on that sphere is actually drawn on a 2D space because we are forced to draw on the edge of the object from one angle; therefore, we can utilize the points on that paint to find the en-face direction because the points on the contour should be orthogonal to that angle we were facing.

4.3 Limitations and future work

The test dataset has small severity subgroups ($n = 7/7/7$), limiting statistical precision and generalizability. Consequently, estimates of agreement (e.g., Bland-Altman bias and limits of agreement) and reliability (ICC) have wide confidence intervals. We also did not validate the pipeline on the external dataset. Furthermore, the study only involved glenoid bones with anterior bone loss, but glenoid bone loss can also occur posteriorly. Magnetic resonance imaging is also commonly used to measure glenoid bone loss and has the advantage of being a noninvasive imaging modality. A future study can use an MRI image

to automate the anterior and posterior measurement of glenoid bone loss and evaluate it on a larger test dataset and an external dataset.

5 CONCLUSION

To our knowledge, this is the first work to automate the measurement of glenoid bone loss on 3D reconstructed CT using linear-based, en-face view, and best-fit circle method. It segments the glenoid and subtracts the humerus bone accurately. This pipeline demonstrates good agreement and reliability with human annotation, and is even better than a human-to-human baseline. It is clinically reliable in automating quantitative measurements, especially in low($< 13.5\%$) and high bone loss($> 20\%$) severity groups for the detection, while human review is required for cases between. In summary, it may be a robust tool in assisting doctors in pre-operative surgical planning for shoulder instability.

References

- [1] W. T. Simonet et al. “Incidence of anterior shoulder dislocation in Olmsted County, Minnesota”. In: *Clin Orthop Relat Res* 186 (1984), pp. 186–191.
- [2] J. L. Boone and R. A. Arciero. “Management of failed instability surgery: how to get it right the next time”. In: *Orthopedic Clinics of North America* 41.3 (2010), pp. 367–379. DOI: [10.1016/j.ocl.2010.02.009](https://doi.org/10.1016/j.ocl.2010.02.009).
- [3] B. D. Owens et al. “Incidence of shoulder dislocation in the United States military: demographic considerations from a high-risk population”. In: *Journal of Bone and Joint Surgery American* 91.4 (2009), pp. 791–796. DOI: [10.2106/JBJS.H.00514](https://doi.org/10.2106/JBJS.H.00514).
- [4] J. F. Griffith. “Measuring glenoid and humeral bone loss in shoulder dislocation”. In: *Quantitative Imaging in Medicine and Surgery* 9 (2019), pp. 134–143. DOI: [10.21037/qims.2019.01.06](https://doi.org/10.21037/qims.2019.01.06).

[5] Alexandra V. Paul et al. "Preoperative planning with three-dimensional CT vs. three-dimensional magnetic resonance imaging does not change surgical management for shoulder instability". In: *JSES Int* 8.2 (2024), pp. 243–249. DOI: [10.1016/j.jseint.2023.08.005](https://doi.org/10.1016/j.jseint.2023.08.005).

[6] R. R. Thacher et al. "Current Concepts in the Measurement of Glenohumeral Bone Loss". In: *Current Reviews in Musculoskeletal Medicine* 16.9 (2023), pp. 419–431. DOI: [10.1007/s12178-023-09852-0](https://doi.org/10.1007/s12178-023-09852-0).

[7] M. A. Rerko et al. "Comparison of various imaging techniques to quantify glenoid bone loss in shoulder instability". In: *J Shoulder Elbow Surg* 22.4 (2013), pp. 528–534. DOI: [10.1016/j.jse.2012.05.034](https://doi.org/10.1016/j.jse.2012.05.034).

[8] Patrícia Martins e Souza et al. "Recurrent anterior glenohumeral instability: The quantification of glenoid bone loss using magnetic resonance imaging". In: *Skeletal Radiol* 43.8 (2014), pp. 1085–1092. DOI: [10.1007/s00256-014-1894-6](https://doi.org/10.1007/s00256-014-1894-6).

[9] Polydoor Emile Huijsmans et al. "Recurrent anterior shoulder instability: accuracy of estimations of glenoid bone loss with computed tomography is insufficient for therapeutic decision-making". In: *Skeletal Radiol* 40.10 (2011), pp. 1329–1334. DOI: [10.1007/s00256-011-1184-5](https://doi.org/10.1007/s00256-011-1184-5).

[10] H. Sugaya et al. "Glenoid rim morphology in recurrent anterior glenohumeral instability". In: *J Bone Joint Surg Am* 85.5 (2003), pp. 878–884. DOI: [10.2106/00004623-200305000-00016](https://doi.org/10.2106/00004623-200305000-00016).

[11] Paolo Baudi et al. "Assessment of bone defects in anterior shoulder instability". In: *Joints* 1.1 (2013), pp. 40–48.

[12] A. J. Bois et al. "Quantifying glenoid bone loss in anterior shoulder instability". In: *Am J Sports Med* 40.9 (2012), pp. 206–212. DOI: [10.1177/0363546512458247](https://doi.org/10.1177/0363546512458247).

[13] Katrin Karpinski et al. "Reliability of Manual Measurements Versus Semiautomated Software for Glenoid Bone Loss Quantification in Patients With Anterior Shoulder Instability". In: *Orthop J Sports Med* 12.2 (2024), p. 23259671231222938. DOI: [10.1177/23259671231222938](https://doi.org/10.1177/23259671231222938).

[14] Marine Launay et al. "Three-Dimensional Quantification of Glenoid Bone Loss in Anterior Shoulder Instability: The Anatomic Concave Surface Area Method". In: *Orthop J Sports Med* 9.6 (2021), p. 23259671211011058. DOI: [10.1177/23259671211011058](https://doi.org/10.1177/23259671211011058).

[15] Avichai Haimi et al. "Automated Quantification of Glenoid Bone Loss in CT Scans for Shoulder Dislocation Surgery Planning". In: *International Journal of Computer Assisted Radiology and Surgery* 19.1 (2024), pp. 129–137. DOI: [10.1007/s11548-023-02995-y](https://doi.org/10.1007/s11548-023-02995-y).

[16] Qingqing Zhao et al. "Glenoid segmentation from computed tomography scans based on a 2-stage deep learning model for glenoid bone loss evaluation". In: *J Shoulder Elbow Surg* 32.12 (2023), e624–e635. DOI: [10.1016/j.jse.2023.05.006](https://doi.org/10.1016/j.jse.2023.05.006).

[17] I. Park, M.-J. Oh, and S.-J. Shin. "Effects of Glenoid and Humeral Bone Defects on Recurrent Anterior Instability of the Shoulder". In: *Clin Orthop Surg* 12.2 (2020), pp. 145–150. DOI: [10.4055/cios19060](https://doi.org/10.4055/cios19060).

[18] Laura E. Keeling et al. "Bone loss in shoulder instability: putting it all together". In: *Annals of Joint* 8.1 (2023), pp. 27–27. DOI: [10.21037/aoj-23-6](https://doi.org/10.21037/aoj-23-6).

[19] J. Chen, Z. Fang, J. Cai, et al. "Glenoid bone loss determination: validity and reliability of the constellation technique versus the sagittal best fit circle technique". In: *Indian J Orthop* 56.10 (2022), pp. 1824–1833. DOI: [10.1007/s43465-022-00720-6](https://doi.org/10.1007/s43465-022-00720-6).

[20] Fabian Isensee et al. "nnU-Net: a self-configuring method for deep learning-based biomedical image segmentation". In: *Nature Methods* 18.2 (2020), pp. 203–211. DOI: [10.1038/s41592-020-01008-z](https://doi.org/10.1038/s41592-020-01008-z).

[21] J. Wasserthal, H.-C. Breit, M. T. Meyer, et al. “TotalSegmentator: robust segmentation of 104 anatomic structures in CT images”. In: *Radiology: Artificial Intelligence* 5.5 (2023), e230024. DOI: [10.1148/ryai.230024](https://doi.org/10.1148/ryai.230024).

[22] S. J. Pan and Q. Yang. “A Survey on Transfer Learning”. In: *IEEE Transactions on Knowledge and Data Engineering* 22.10 (Oct. 2010), pp. 1345–1359. DOI: [10.1109/TKDE.2009.191](https://doi.org/10.1109/TKDE.2009.191).

[23] Grzegorz Chlebus et al. “Automatic liver tumor segmentation in CT with fully convolutional neural networks and object-based postprocessing”. In: *Scientific Reports* 8.1 (Oct. 19, 2018), p. 15497. DOI: [10.1038/s41598-018-33860-7](https://doi.org/10.1038/s41598-018-33860-7).

[24] Lukas P. E. Verweij et al. “Accuracy of Currently Available Methods in Quantifying Anterior Glenoid Bone Loss: Controversy Regarding Gold Standard—A Systematic Review”. In: *Arthroscopy* 36.8 (2020), 2295–2313.e1. DOI: [10.1016/j.arthro.2020.04.012](https://doi.org/10.1016/j.arthro.2020.04.012).

[25] Andrew L. Maas, Awni Y. Hannun, and Andrew Y. Ng. “Rectifier Nonlinearities Improve Neural Network Acoustic Models”. In: *Proceedings of the 30th International Conference on Machine Learning (ICML Workshop on Deep Learning for Audio, Speech, and Language Processing)*. Atlanta, GA, USA, 2013, p. 3.

[26] Zhen-Hua Feng et al. “Wing Loss for Robust Facial Landmark Localisation with Convolutional Neural Networks”. In: *Proceedings of the IEEE Conference on Computer Vision and Pattern Recognition (CVPR)*. IEEE. 2018, pp. 2235–2245.

[27] Xinyao Wang, Liefeng Bo, and Li Fuxin. “Adaptive Wing Loss for Robust Face Alignment via Heatmap Regression”. In: *Proceedings of the IEEE International Conference on Computer Vision (ICCV)*. Oct. 2019, pp. 6971–6981.

[28] Diederik P. Kingma and Jimmy Ba. “Adam: A Method for Stochastic Optimization”. In: *Proceedings of the 3rd International Conference on Learning Representations (ICLR)*. arXiv:1412.6980. 2015.

[29] Gunilla Borgefors. “Distance Transformations in Digital Images”. In: *Computer Vision, Graphics and Image Processing* 34.3 (1986), pp. 344–371. DOI: [10.1016/S0734-189X\(86\)80047-0](https://doi.org/10.1016/S0734-189X(86)80047-0).

[30] Haoqiang Fan, Hao Su, and Leonidas J. Guibas. “A Point Set Generation Network for 3D Object Reconstruction from a Single Image”. In: *Proceedings of the IEEE Conference on Computer Vision and Pattern Recognition (CVPR)*. 2017, pp. 2463–2471. DOI: [10.1109/CVPR.2017.264](https://doi.org/10.1109/CVPR.2017.264).

[31] Ta-Chih Lee, Rangasami L. Kashyap, and Chong-Nam Chu. “Building Skeleton Models via 3-D Medial Surface/Axis Thinning Algorithms”. In: *Computer Vision, Graphics, and Image Processing* 56.6 (1994), pp. 462–478. DOI: [10.1006/cgip.1994.1042](https://doi.org/10.1006/cgip.1994.1042).

[32] Hailong Zhang et al. “Establishment of a True En Face View in the Evaluation of Glenoid Morphology for Treatment of Traumatic Anterior Shoulder Instability”. In: *Arthroscopy* 36.3 (2020), pp. 668–679. DOI: [10.1016/j.arthro.2019.10.036](https://doi.org/10.1016/j.arthro.2019.10.036).

[33] David Kovacevic, Justin L. Hodgins, and Louis U. Bigliani. “Lucent lines and glenoid components: What do they portend?” In: *Seminars in Arthroplasty* 25.4 (2014), pp. 277–285. DOI: [10.1053/j.sart.2015.02.008](https://doi.org/10.1053/j.sart.2015.02.008).